

A $0.2 M_{\odot}$ PROTOSTAR WITH A KEPLERIAN DISK IN THE VERY YOUNG L1527 IRS SYSTEM

John J. Tobin¹, Lee Hartmann², Hsin-Fang Chiang^{3,4}, David J. Wilner⁵ and Leslie W. Looney³, Laurent Loinard^{6,7}, Nuria Calvet², Paola D'Alessio⁶

¹Hubble Fellow, National Radio Astronomy Observatory, Charlottesville, VA 22903; jto-
bin@nrao.edu

²Department of Astronomy, University of Michigan, Ann Arbor, MI 48109

³Department of Astronomy, University of Illinois, Urbana, IL 61801

⁴Institute for Astronomy and NASA Astrobiology Institute, University of Hawaii at Manoa, Hilo, HI 96720

⁵Harvard-Smithsonian Center for Astrophysics, Cambridge, MA 02138

⁶Centro de Radioastronomía y Astrofísica, UNAM, Apartado Postal 3-72 (Xangari), 58089 Morelia, Michoacán, México

⁷Max-Planck-Institut für Radioastronomie, Auf dem Hügel 69, 53121 Bonn, Germany

In their earliest stages, protostars accrete mass from their surrounding envelopes through circumstellar disks. Until now, the smallest observed protostar/envelope mass ratio was ~ 2.1 [1]. The protostar L1527 IRS is thought to be in the earliest stages of star formation[2]. Its envelope contains $\sim 1 M_{\odot}$ of material within a ~ 0.05 pc radius[3, 4], and earlier observations suggested the presence of an edge-on disk[5]. Here we report observations of dust continuum emission and ^{13}CO ($J = 2 \rightarrow 1$) line emission from the disk around L1527, from which we determine a protostellar mass of $M_* = 0.19 \pm 0.04 M_{\odot}$ and a protostar/envelope mass ratio of ~ 0.2 . We conclude that most of the luminosity is generated through the accretion process, with an accretion rate of $\sim 6.6 \times 10^{-7} M_{\odot} \text{ yr}^{-1}$. If it has been accreting at that rate through much of its life, its age is $\sim 300,000$ yr, though theory suggests larger accretion rates earlier[6], so it may be younger. The presence of a rotationally-supported disk is confirmed and significantly more mass may be added to its planet-forming region as well as the protostar itself.

The protostar L1527 IRS (hereafter L1527) in the Taurus cloud, at a distance of about 140 pc, is one of the nearest Class 0 protostars. This is the earliest phase of the star formation process[2] and we show a schematic diagram of a protostellar system in Figure 1. Observations of dust continuum emission toward L1527 were obtained with the Submillimeter Array (SMA) and Combined Array for Millimeter-wave Astronomy (CARMA) at $\lambda = 870 \mu\text{m}$, 1.3 mm, and 3.4 mm. The 870 μm and 3.4 mm data are shown in Figure 2 with sufficient resolution to resolve the emission from the disk midplane, finding it to be extended north-south, like the 3.8 μm dark lane. The observed disk size is $\sim 180 \text{ AU} \pm 12 \text{ AU}$ in diameter ($R \sim 90 \text{ AU}$), measured from inside the outer contour plotted in Figure 2; the dust emission appears smaller than the mid-infrared dark lane because the lower density outer disk is

fainter than the sensitivity limit. Other studies did not conclusively detect a disk around L1527 or other Class 0 protostars because the spatial resolution was too low to distinguish the disk emission from the envelope and/or the disks were too small[7, 8]. We estimate a disk mass of $0.007 \pm 0.0007 M_{\odot}$ from the $\lambda = 870 \mu\text{m}$ flux density ($F_{870\mu\text{m}} = 213.6 \pm 8.1 \text{ mJy}$); details are given in Section 3 of the Supplementary Information. We consider this mass a lower limit because the adopted dust opacity is large[9], and we have not accounted for spatial filtering by the interferometer.

We observed the ^{13}CO ($J = 2 \rightarrow 1$) molecular line transition with CARMA at 1.3 mm. This line traces the outflow in most Class 0 protostars[10]; however, Figure 3 shows that the ^{13}CO emission primarily traces the inner envelope and disk in L1527. The outflow is detected at velocities less than $\pm 1 \text{ km s}^{-1}$, but does not affect our analysis, see Section 2 of the Supplementary Information. The ^{13}CO data have lower resolution than the $870 \mu\text{m}$ and 3.4 mm observations ($1''$, 140 AU); however, the positional accuracy of line emission is comparable to the resolution divided by signal-to-noise ratio (typically 5 or higher), enabling us to determine the location of emission accurately in each velocity channel. Figure 3 shows the ^{13}CO emission from the blue and redshifted components to be on opposite sides of protostar, consistent with Keplerian rotation. The emission from the disk is most likely confined to $\pm 1''$; at larger radii and lower velocities we expect the flattened envelope to contribute to the kinematics as shown by lower resolution ^{13}CO ($J = 1 \rightarrow 0$) observations[11]. The observations shown in Figures 2 and 3 as a whole provide definitive evidence for a large, rotationally-supported disk in this Class 0 protostellar system. Such a disk at this early phase may be inconsistent with some disk formation models that consider strong magnetic braking[12, 13]; however, large disks can form at this stage in models with weak magnetic fields[14, 15] or if the magnetic field is not aligned with the rotation axis[16].

Assuming that the disk is rotationally-supported and that the mass of the protostar is dominant, we can use the position-velocity information from the molecular line data to determine the protostellar mass. This has been done for more evolved sources, but not a Class 0 protostar[17, 18]. To determine the mass, we measured the positional offset of the line emission relative to the protostar (1.3 mm continuum source) in each velocity channel (binned to 0.3 km s^{-1}) and the position-velocity data are fit with a Keplerian rotation curve ($v = (GM/r)^{1/2}$). These data are plotted in Figure 4 and least-squares fitting yields a protostellar mass of $0.19 \pm 0.04 M_{\odot}$; the flattening of radius at velocities less than $\sim 1.5 \text{ km s}^{-1}$ can be attributed to the superposition of rotation velocities projected along the line of sight at large radii. We do not expect contributions from the envelope to affect the fit because its emission is at lower velocities and larger-scales[11]. The edge-on nature of L1527 facilitates this analysis because the $\sim 85^\circ$ inclination[19, 5] does not significantly affect any calculations. Although the model fit in Figure 4 is simplistic, it highlights the important physics of the problem, and the method is consistent with simulated observations of more complicated line radiative transfer models that require many assumptions, see Section 4 of the Supplementary Information.

Masses have previously been estimated for binary Class 0 protostellar systems using proper motion measurements at very high resolution[20], but with substantial uncertainty due to unconstrained orbital parameters. The primary uncertainty in our measurement is whether the protostellar mass is dominant over the disk/envelope mass at the scales we are probing. The disk mass of $0.007 M_{\odot}$ could be up to a factor of a few higher due to opacity uncertainties

and the envelope mass within $R = 150$ AU is only expected to be $\sim 0.01 M_{\odot}$ since most mass is on large-scales. If we allow for a factor of four higher disk and envelope masses, they would combine to contribute at most $\sim 35\%$ to the total mass. The kinematic effect of this additional mass should become apparent at larger disk radii, but the current data are insufficient to distinguish this effect. Moreover, the possibility of additional mass would only cause the protostellar mass to be overestimated.

The ratio of protostellar mass to envelope mass in L1527 is only $\sim 20\%$; all other protostellar systems with dynamical mass measurements from disk rotation have protostellar masses greater than twice the surrounding envelope mass[1]. Therefore, in contrast to these more evolved systems, L1527 will likely accumulate significantly more mass. Accreting protostars are expected to follow a ‘birthline’ with rising effective temperature and luminosity with increasing mass; the birthline is also the starting point of pre-main sequence evolution once the protostar has stopped accreting significantly[21]. If L1527 is on the birthline, we can estimate its stellar parameters from the mass. We use the birthline model with an accretion rate of $2 \times 10^{-6} M_{\odot} \text{ yr}^{-1}$; for a $0.19 M_{\odot}$ protostar, this model indicates a radius of $1.7 R_{\odot}$, effective temperature of 3300 K, and a luminosity of $0.3 L_{\odot}$ [21]. This indicates that $\sim 90\%$ of the 2.75 solar luminosities[19] is supplied by accretion of mass onto the protostar. Thus, the accretion rate of the disk onto the protostar is $\sim 6.6 \times 10^{-7} M_{\odot} \text{ yr}^{-1}$, assuming $L_{\text{acc}} = G\dot{M}/R_*$. If the protostar has been accreting at this rate throughout its life, its age is only $\sim 300,000$ yr, within the expected lifetime of the Class 0 phase[22]. However, theoretical studies indicate that mass infall/accretion rates may be larger initially and decrease with time[6]; in addition, protostars are expected to have variable accretion rates[23], so L1527 could be younger. The dynamical time of the 0.3 pc outflow (red and blue sides) as measured by a recent survey of Taurus is $\sim 30,000$ yr[24].

The detection of a proto-planetary disk and a measurement of protostellar mass have made L1527 one of the best characterized Class 0 protostellar systems known. Its high accretion rate is nearly a factor of 100 greater than the more evolved pre-main sequence stars with disks; this rate is high enough to heat the inner disk to temperatures consistent with early Solar System conditions[25]. While we cannot say definitively what L1527 will look like at the end of its formation phase, it does have the potential to gain as much mass as the sun from its envelope and it already has a proto-planetary disk with at least 7 Jupiter masses, similar to presumed planet forming disks[26]. Therefore, L1527 already has all the elements of a solar system in the making.

Acknowledgments: We thank the anonymous referees for constructive comments that have improved the quality of the manuscript. The authors wish to thank E. Bergin for commenting on the manuscript and W. Kwon for discussing improvements to the data reduction. J. Tobin acknowledges support provided by NASA through Hubble Fellowship grant #HST-HF-51300.01-A awarded by the Space Telescope Science Institute, which is operated by the Association of Universities for Research in Astronomy, Inc., for NASA, under contract NAS 5-26555. L. H. and J. T. acknowledge partial support from the University of Michigan. H.-F. C. acknowledges support from the National Aeronautics and Space Administration through the NASA Astrobiology Institute under Cooperative Agreement No. NNA09DA77A issued through the Office of Space Science. L.W.L. and H.-F. C. acknowledge support from the Laboratory for Astronomical Imaging at the University of Illinois and the NSF under grant AST-07-09206. P. D. acknowledges a grant from PAPIIT-UNAM. L. L. acknowledges

the support of DGAPA, UNAM, CONACyT (México), and the Alexander von Humboldt Stiftung for financial support. Support for CARMA construction was derived from the states of Illinois, California, and Maryland, the James S. McDonnell Foundation, the Gordon and Betty Moore Foundation, the Kenneth T. and Eileen L. Norris Foundation, the University of Chicago, the Associates of the California Institute of Technology, and the National Science Foundation. Ongoing CARMA development and operations are supported by the National Science Foundation under a cooperative agreement, and by the CARMA partner universities. The Submillimeter Array is a joint project between the Smithsonian Astrophysical Observatory and the Academia Sinica Institute of Astronomy and Astrophysics and is funded by the Smithsonian Institution and the Academia Sinica. The National Radio Astronomy Observatory is a facility of the National Science Foundation operated under cooperative agreement by Associated Universities, Inc.

Contributions: J.T., H.-F.C., D.J.W., and L.W.L. participated in data acquisition and reduction. All authors contributed to the data analysis, discussed the results, and commented on the manuscript.

Reprints and permissions information is available at www.nature.com/reprints

Competing financial interests: The authors declare no competing financial interests.

Corresponding Author: Correspondence and requests for materials should be addressed to John J. Tobin; jtobin@nrao.edu.

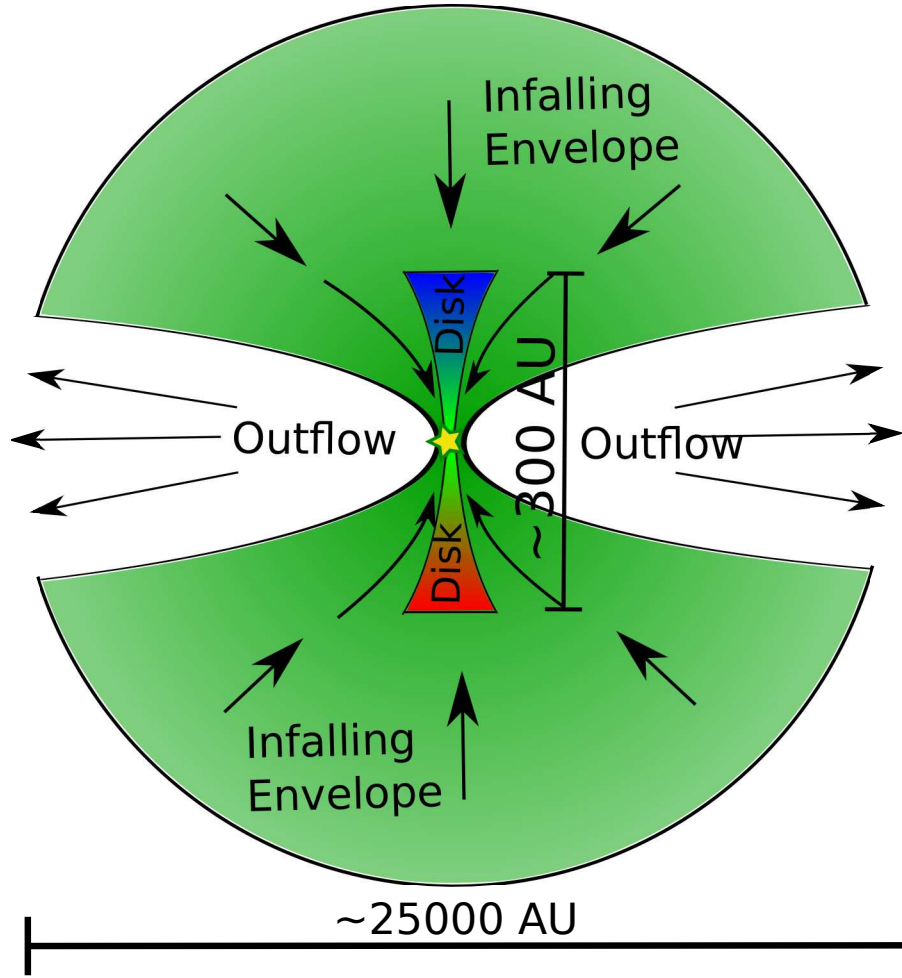


FIGURE 1. Cartoon of a protostellar system rotated to match the orientation of L1527. The green highlights the large ($R \sim 12,500$ AU) infalling envelope surrounding the protostar and disk; the envelope geometry on 10,000 AU scales is generally more complex than shown here[27]. Because the infalling material has some net rotation, it falls onto a disk due to conservation of angular momentum rather than directly onto the protostar. The disk is colored with a red to blue velocity gradient to illustrate Keplerian rotation around the protostar. Mass is transported from the envelope to the disk and then it is accreted through the disk and onto the protostar. The protostar and disk both work together and drive a bipolar outflow[10] which evacuates the polar regions of the envelope. AU is an abbreviation for astronomical unit, the distance from the earth to the sun which is 1.496×10^{13} cm.

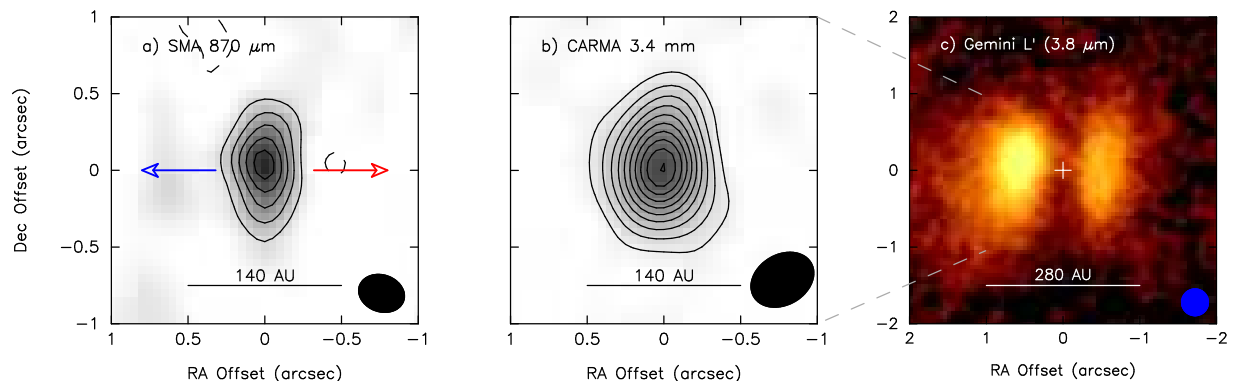


FIGURE 2. Images of the edge-on disk around the protostar L1527. High-resolution images of L1527 are shown at wavelengths of $870\ \mu\text{m}$ from the SMA (a), $3.4\ \text{mm}$ from CARMA (b), and $3.8\ \mu\text{m}$ from Gemini (c), showing the disk in dust continuum emission and scattered light. The Gemini image is shown on a larger scale to fully capture the scattered light features, the dashed gray lines mark the outer edge of the region shown in the sub/millimeter images. The sub/millimeter images are elongated in the direction of the dark lane shown in panel (c), consistent with an edge-on disk in this Class 0 protostellar system. The outflow direction is indicated by the red and blue arrows in panel (a), denoting the respective directions of the outflow. The white cross in panel (c) marks the central position of the disk from the SMA images. The contours in the $870\ \mu\text{m}$ and $3.4\ \text{mm}$ images start at 3 times the noise level and increase at this interval; the noise level is $5.0\ \text{mJy beam}^{-1}$ and $0.24\ \text{mJy beam}^{-1}$ for the SMA and CARMA data respectively. The ellipses in the lower right corner of each image gives the resolution of the observations, approximately $0.25''$, $0.35''$, and $0.35''$ in the left, middle, and right panels respectively.

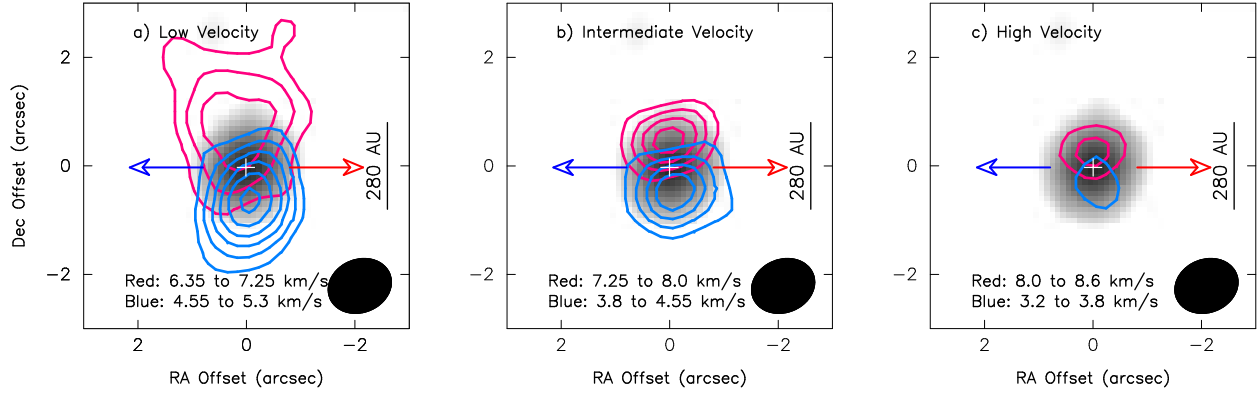


FIGURE 3. ^{13}CO emission from the disk around L1527 exhibiting a Keplerian rotation signature. The CARMA 1.3 mm continuum image is shown (grayscale) with the red and blue contours showing ^{13}CO emission integrated at low velocities (a), intermediate velocities (b), and high velocities (c). The white cross in all panels marks the location of the protostar. The blue and red-shifted emission centroids show a clear signature of rotation on the size-scale of the protostellar disk and no extension of emission along the outflow. The low-velocity emission likely includes contributions from the envelope, while the intermediate to high-velocity emission is dominated by the disk. The low-velocity range is from 6.35 km s^{-1} to 7.25 km s^{-1} and 4.55 km s^{-1} to 5.3 km s^{-1} ; the intermediate velocity range is from 7.25 km s^{-1} to 8.0 km s^{-1} and 3.8 km s^{-1} to 4.55 km s^{-1} ; the high velocity range is from 8.0 km s^{-1} to 8.6 km s^{-1} and 3.2 km s^{-1} to 3.8 km s^{-1} . The contours start and increase in intervals 3 times noise level (σ) where $\sigma = 0.85 \text{ K km s}^{-1}$ (red) and 0.75 K km s^{-1} (blue). The angular resolution of these data are given by the ellipse in the lower right corners, $1.1'' \times 0.95''$.

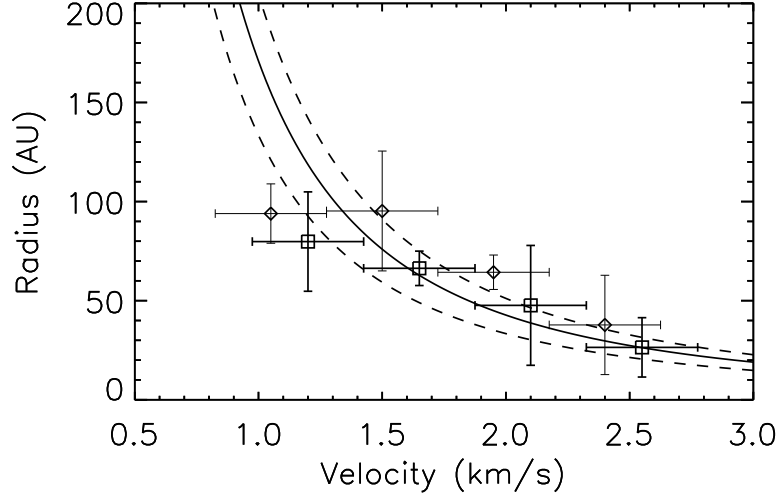


FIGURE 4. Radius versus velocity plots showing the rotation curve derived from the ^{13}CO emission. Rotationally supported motion around a central point mass will have a velocity equal to $(GM/r)^{1/2}$. This function was fit to the data, finding a best fitting mass of $M_* = 0.19 \pm 0.04 M_\odot$. We used line radiative transfer models to confirm that this method yields reliable protostellar masses with simulated data at the same resolution, see Section 4 of the Supplementary Information. The velocity profile for the best fitting mass is shown as the solid line and the dashed lines show the 1σ uncertainty level. The diamonds are data on the south, blue-shifted side of the disk and the squares are data on the north, red-shifted side of the disk. The uncertainty in the observed data points is derived from the fixed velocity channel width (x-axis) and error in the radius (y-axis) is the 1σ error derived from adding in quadrature the positional uncertainty of the Gaussian fit to the ^{13}CO emission and the error in the position of the protostellar source. The flattening of the data points at velocities less than 1.5 km s^{-1} is due to the superposition of rotation velocities projected to our line of sight at large disk radii and also witnessed in the data from the line radiative transfer models, see Section 4 of the Supplementary Information.

SUPPLEMENTARY INFORMATION

1. OBSERVATIONS

The data presented in this work were taken with both the Combined Array for Research in Millimeter Astronomy (CARMA)[28] and the Submillimeter Array (SMA)[29], both of which are sub/millimeter interferometer arrays. CARMA is a heterogeneous array comprised of six 10.4 m antennas, nine 6 m antennas, and eight 3.5 m antennas at Cedar Flat California in the Inyo Mountains. The 1.3 mm data were taken in C and D configurations which provide angular resolutions of $\sim 1''$ and $\sim 2.5''$ respectively and the 3.4 mm data were taken in A configuration which provides an angular resolution of $\sim 0.35''$. The SMA is an array of eight 6 m antennas at Mauna Kea and data were taken in the very extended configuration with a resolution of $\sim 0.25''$.

1.1 CARMA 1.3 mm Observations and Data Reduction. The 1.3 mm C-array observations were conducted on 2012 Jan 29, Feb 04, Feb 06, and Feb 09 using the 10.4 m and 6 m antennas. The local oscillator was tuned to $\nu=223.01$ GHz and four 500 MHz bands were configured for continuum observation. The IF range spans 1 to 9 GHz and the receivers operate in dual-sideband (DSB) mode yielding 4 GHz of bandwidth in one polarization. The remaining spectral windows were configured to observe ^{13}CO , ^{12}CO , C^{18}O , and H_2CO . The Jan 29 data had excellent phase coherence throughout the track, while the Feb 04, 06, and 09 data had periods of poor phase coherence. 3C111 was observed as the gain calibrator, Uranus was the flux calibrator, and 3C111 or 3C84 were used as bandpass calibrators. L1527 was observed in D-array on 2009 Aug 27 with the local oscillator tuned to $\nu=223.1212$ GHz, two 500 MHz bands were configured for continuum observation (2GHz DSB) and one spectral window was centered on the ^{13}CO line. 3C111 was observed as the gain calibrator, Uranus was the flux calibrator, and 3C84 was the bandpass calibrator.

The data were reduced using the MIRIAD software package [30]. The visibilities were first corrected for the updated baseline solution and transmission line length correction. Then the amplitudes and phases were examined for each baseline, flagging the source observations between points where the calibrator had bad amplitudes or extremely high phase variance. The data were then bandpass corrected using the *mfcal* task. The absolute flux calibration was calculated using the *bootflux* task to determine the flux of 3C111 relative to the absolute flux calibrator. We compared the visibility amplitudes of L1527 in ranges of overlapping uv-coverage to estimate our flux calibration uncertainty. The data had systematic offsets necessitating rescaling and we estimate an absolute flux uncertainty at 1.3 mm of 20%; however, the rescaling only affects the absolute intensity scale and not the structure of emission.

The data were then imaged by first computing the inverse Fourier transform of the data with the *invert* task, weighting by system temperature and creating the dirty map. The dirty map is then CLEANed using the *mossdi* task down to $1.5\times$ the RMS noise level and the image is restored and convolved with the CLEAN beam by the *restor* task. This procedure was repeated for each channel in the spectral line image cube and the continuum images were averaged over the entire bandwidth.

1.2 CARMA 3.4 mm Observations and Data Reduction. The 3.4 mm A-array observations of L1527 were taken on 2010 December 02 during stable conditions with $\sim 4\text{mm}$

of precipitable water vapor (pwv) using the 10.4 m and 6 m antennas. The local oscillator was tuned to $\nu=90.7510$ GHz and the correlator was configured for 4-bit sampling with 8 - 500 MHz moveable spectral windows, measuring continuum emission. We arranged windows such that they occupied the 1 to 5 GHz range of IF bandwidth and our full instantaneous bandwidth was 8 GHz in one polarization. The primary gain calibrator was 3C111, 12.8 degrees away on the sky, 0431+206 was observed as a test source in conjunction with L1527. 3C84 was observed as the bandpass calibrator, and Neptune was observed as the absolute flux calibrator. We estimate an absolute flux uncertainty of 10%. The observations were conducted in a standard loop, observing 3C111 for 3 minutes, L1527 for 7 minutes, 0431+206 for 1 minute, and then repeating. Pointing was updated periodically using optical pointing correction and radio pointing was done once during the track.

The data were reduced in a similar way to the 1.3 mm data; however we also used the CARMA paired antenna calibration system (C-PACS)[31] was used for enhanced atmospheric phase correction in the A configuration. Briefly, the C-PACS calibration works as follows, the eight 3.5 meter dishes are positioned next to the 10.4 meter and 6 meter antennas at the longest baselines. While the source(s) is being observed, the 3.5 meter dishes are observing a nearby calibrator at 30 GHz. The short timescale phase variations during the observation of the source(s) are corrected from the simultaneous calibrator observations by the 3.5 meter antennas. This correction effectively reduces the atmospheric decorrelation at the longest baselines, so long as the C-PACS calibrator is sufficiently close to the source(s). During the A-array observation of L1527, the C-PACS antennas observed the quasar 0428+329 which was 7.4° away on the sky with a flux density of 1.9 Jy at 30 GHz.

The data were imaged in the same way as the 1.3 mm data, but we also reconstructed images of the test source 0431+206, confirming the good 3.4 mm “seeing.”

1.3 Submillimeter Array Observations and Data Reduction. We observed L1527 with the SMA on the nights of 2011 January 5 and 6 in very extended configuration, with 7 antennas operating. The first track had excellent phase coherence but the precipitable water vapor (pwv) was ~ 4.0 mm and the second track had ~ 2.0 mm pwv, but worse phase coherence. The local oscillator was tuned to $\nu=347.02$ GHz and the correlator was used in 4 GHz (DSB) mode. The correlator was configured for 32 channels per chunk, the coarsest resolution mode for continuum observations, each chunk is 104 MHz wide and there are 48 correlator chunks. 3C111 was observed as the gain calibrator, 0510+180 was observed as a secondary calibrator, 3C279 was the bandpass calibrator, and Callisto was the absolute flux calibrator. The data were taken in the following loop: 3C111 was observed for 2.5 minutes, then L1527 was observed for 8 minutes, then 0510+180 was observed for 2.5 minutes, then L1527 again and finishing with 3C111.

The data were reduced using the MIR package, an IDL-based software package originally developed for the Owens Valley Radio Observatory and adapted by the SMA group. The data were first corrected for the updated baseline solutions and then phases and amplitudes on each baseline were inspected and uncalibrateable data were flagged. The system temperature correction was then applied to the data and the bandpass correction was calculated, trimming three channels at the edge of each correlator chunk. After bandpass calibration, a first-pass gain calibration was performed on 3C111, 0510+180, and Callisto to measure the calibrator fluxes. The L1527 and 0510+180 data were then calibrated for amplitude and phase using only 3C111. We estimate an absolute flux uncertainty of 10%. The data were

then exported to MIRIAD and were imaged using the same technique as outlined for the CARMA data. 0510+180 was also imaged and found to be a point source, confirming the excellent submillimeter seeing conditions.

2. ORIGIN OF ^{13}CO EMISSION

It is well known that ^{13}CO frequently traces outflow activity in Class 0 protostars[10]. However, we have found the ^{13}CO emission to trace disk rotation in L1527, therefore it is important to rule-out outflow contamination. Figure S1 shows the ^{13}CO ($J = 2 \rightarrow 1$) channel maps in 0.3 km s^{-1} bins at velocities between 3.5 km s^{-1} and 8.0 km s^{-1} . The wide-angle outflow is apparent as the large “X” across the image with substantial spatial filtering; similar in structure to the outflow cavities traced in HCO^+ [32]. The outflow only appears at low velocities ($\pm 1.3 \text{ km s}^{-1}$ from line center at 5.9 km s^{-1}). We also detect the flattened envelope structure previously imaged in ^{13}CO ($J = 1 \rightarrow 0$) between velocities of 5.3 and 6.5 km s^{-1} [11]. The emission does not appear as extended as in the previous works due to our observations having higher spatial resolution, thus more spatial filtering of emission. Moreover, the previous studies had a larger field of view, $\sim 60''$ versus $\sim 30''$ in our data.

The signature of disk rotation is found in the compact emission present in all channels with velocities greater than $\pm 0.6 \text{ km s}^{-1}$ from line center. The emission is offset normal to the outflow and the red and blue-shifted emission is on opposite sides of the continuum source, orthogonal to the outflow direction. The spatial offsets of the higher velocity emission near the protostar are strong evidence that the ^{13}CO emission at small-scales is tracing the disk and not outflow emission. There may be some blending of outflow/envelope emission with the disk at velocities less than $\pm 0.6 \text{ km s}^{-1}$, but outside of this range the emission from the compact disk is quite distinct.

3. DISK MASS

If the sub/millimeter emission of L1527 is optically thin and isothermal, then the mass of the disk can be estimated directly from its measured flux, provided that the temperature is known. Following previous work on disk masses[9], we assume a dust opacity law with a spectral index (β) of 1[33], normalized to $\kappa_0 = 0.035 \text{ g cm}^{-2}$ at $850 \mu\text{m}$ [9], assuming a dust-to-gas mass ratio of 1:100. We then calculate the mass assuming optically thin emission and constant dust temperature with the equation

$$(1) \quad M_{\text{dust}} = \frac{D^2 F_\lambda}{\kappa_0 \left(\frac{\lambda}{850 \mu\text{m}} \right)^{-\beta} B_\lambda(T_{\text{dust}})},$$

where $\beta = 1$, $D = 140 \text{ pc}$ and T_{dust} is estimated to be 30 K [9]. The integrated flux densities at $870 \mu\text{m}$ and 3.4 mm were $213.6 \pm 8.1 \text{ mJy}$ and $16.9 \pm 1.4 \text{ mJy}$. This yields a masses of $0.007 \pm 0.0007 M_\odot$ at $870 \mu\text{m}$ and $0.025 \pm 0.003 M_\odot$ with the propagation of statistical error and 10% absolute calibration uncertainty. The uncertainty in this calculation is dominated by our assumptions of the dust mass opacity, β , and characteristic dust temperature. The dust opacity could be a factor of a few lower[34, 35, 5] which would raise the mass by the same factor and a change in dust temperature of $\pm 10 \text{ K}$ lowers/raises the disk mass by a factor of ~ 1.3 . The difference in mass between the $870 \mu\text{m}$ measurement and the 3.4 mm suggests that either the emission is optically thick at $870 \mu\text{m}$ or the dust opacity has

a shallower spectral index than assumed. There is evidence that β may be shallower than 1, if we also consider the recent 7 mm flux measurement from the EVLA[36], the spectral slope of emission from 870 μm , 3.4 mm, and 7 mm is consistent with $F_\nu \propto \nu^2$. In the main text, we only list the 870 μm mass because it is least affected by the assumption of β and is directly comparable to previous work[9] and exploration of the dust opacity properties of the disk is beyond the scope of this paper.

4. KINEMATIC MODELING

In order to better constrain the protostellar mass of L1527, we calculated radiative transfer models of the ^{13}CO emission using the Line Modeling Engine (LIME), a Monte Carlo spectral line and dust continuum radiative transfer code[37]. The temperature and density structure of the envelope and disk is calculated by another radiative transfer code written by Barbara Whitney that calculates the propagation of luminosity through the envelope and protostellar disk[38].

We have adopted the envelope density and velocity structure from the rotating collapse model[39, 40, 41]. This density structure is spherically symmetric at large radii, but near centrifugal radius (R_C) the envelope becomes flattened due to rotation; the envelope density is normalized to a fiducial density at a radius of 1 AU ($\rho_{1\text{AU}}$). The velocities consider infall and rotation under the assumption that the central protostellar mass is dominant, in other words we ignore any contributions of mass from the envelope and/or disk. The infalling envelope becomes rotationally supported at the centrifugal radius (R_C), assumed to be equal to the disk radius. Outflow cavities are also included in this model with an opening angle of 20° . The disk model is parametric; we define the radial density profile, flaring as a function of disk radius, an initial scale height, and total mass. We also assume a Gaussian vertical disk structure. The envelope is assumed to have $\rho_{1\text{AU}} = 7.25 \times 10^{-14} \text{ g cm}^{-3}$, the disk mass is $0.01 M_\odot$, the disk radius is 150 AU, the disk flaring H is proportional to $R^{1.3}$ and a scale height at 100 AU of 40 AU. The infall rate implied by the rotating collapse model is $7 \times 10^{-6} M_\odot \text{ yr}^{-1}$ when adjusted for the measured protostellar mass. These parameters are selected from disk models constructed for L1527 that fit the sub/millimeter data, Gemini imaging, and SED[5, 42]. Note that the combined envelope and disk masses for this model are only $0.02 M_\odot$ out to $R = 420 \text{ AU}$ ($3''$).

The ^{13}CO abundance is assumed to be 1.66×10^{-5} per Hydrogen molecule, where the dust temperature is greater than 20 K. This assumes a standard CO abundance[43] with a $^{13}\text{CO}/\text{CO}$ ratio of 1/60. We assume that all CO is frozen onto dust grains at temperatures less than 20 K. The density structure of the envelope models does not depend on the protostellar mass, therefore mass can be varied independently of the envelope. We calculated LIME models for protostellar masses between 0.025 and $0.3 M_\odot$ in $0.0125 M_\odot$ intervals to compare with the observed ^{13}CO kinematics. On scales less than $1''$ most of the emission is from the disk, while on $2''$ to $3''$ scales the emission originates in the inner envelope. However, the rotation velocities of the envelope are becoming comparable to the infall velocities on these scales[39].

Each model was run through a simulated observation with the *simdata* task of the CASA software package*. This calculates the Fourier transform of the emission in each velocity

*<http://casa.nrao.edu>

channel, samples it with uv-coverage similar to what is provided by the CARMA C and D configurations at 1.3 mm, and then reconstructs the image from the inverse Fourier transform and the CLEAN algorithm.

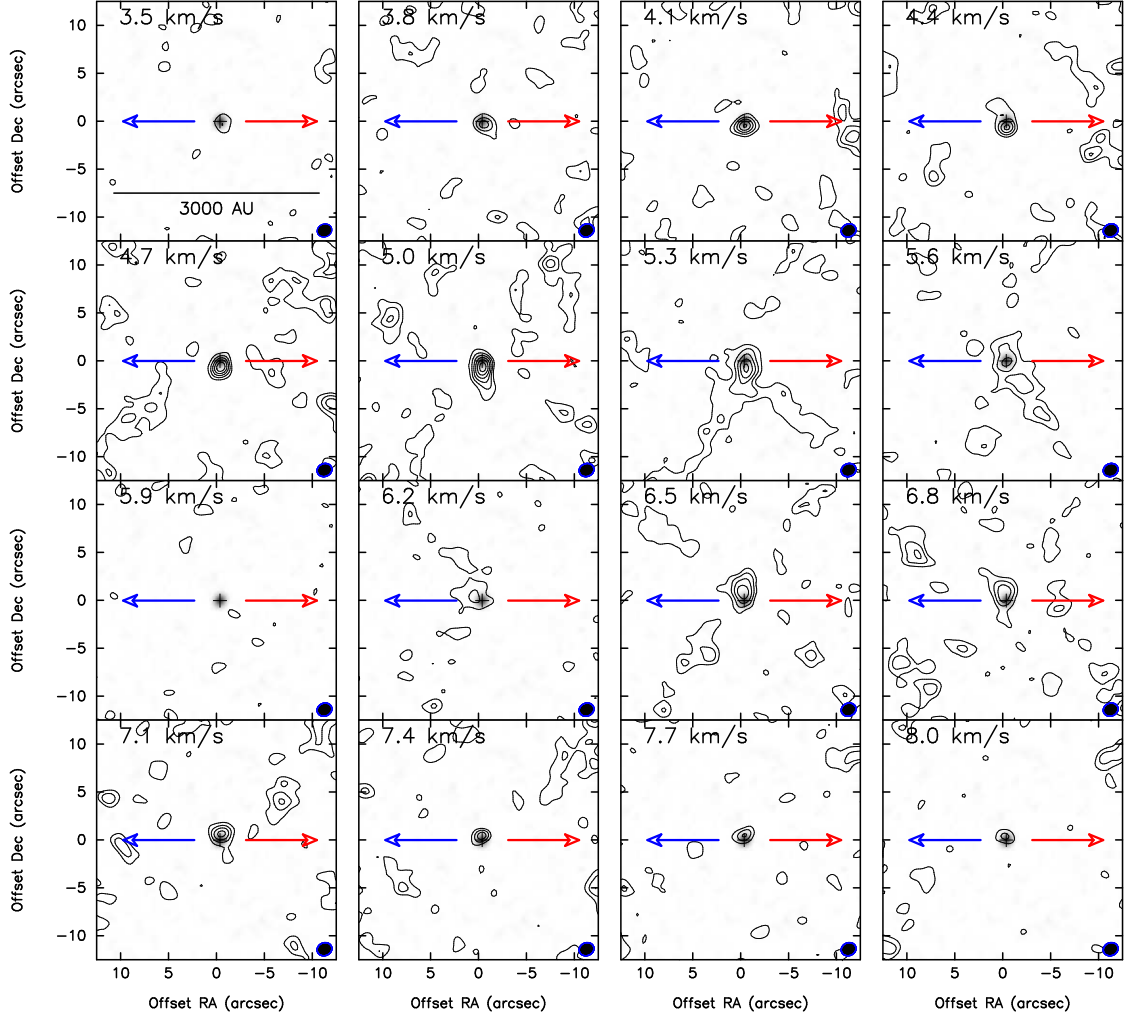
We compared the observations to the models in two ways. The first method was the same as used in the main paper to fit the mass of the protostar. This was done by calculating the centroid of the line emission offset from the protostar at a given velocity within a velocity range of 0.5 to 3.0 km s⁻¹. This enabled us to verify that the method used to derive the mass of L1527 was reliable, using models with a known protostellar mass. The models masses derived from the least-squares fits versus actual model masses are given in Table S1, showing that a model with an actual mass of 0.225 M_{\odot} has a mass fit of $M_{fit} = 0.19 M_{\odot}$, slightly underestimating the true mass of the model. Thus, the mass of L1527 could be closer to 0.225 M_{\odot} ; however, this is already within the statistical uncertainty of the least-squares fit. The model data points are overlaid on the observations in Figure S2 and agree very well with the positions and velocities of the observed data. Position-velocity diagrams of the ¹³CO emission for L1527 and the $M_{*} = 0.225 M_{\odot}$ model are shown in Figure S3. While the data are noisy and have some emission asymmetries, the plots qualitatively agree. This indicates that a disk and a infalling/rotating envelope[39, 40] describe the velocity structure quite well at these small-scales.

The second method we used to derive the mass of L1527 involved subtracting the model emission from the data in each velocity channel and calculating

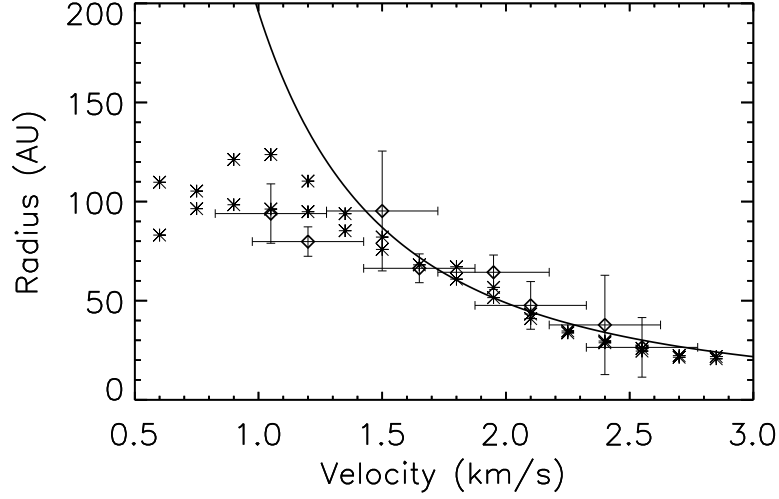
$$(2) \quad \chi^2 = \sum_{\alpha, \delta, v}^N \frac{(I_{obs}(\alpha, \delta, v) - I_{model}(\alpha, \delta, v))^2}{\sigma_i^2}.$$

χ^2 is calculated within a 2'' (α) \times 4'' (δ) region centered on the protostar in the velocity ranges between 3.5 km s⁻¹ < V < 4.7 km s⁻¹ and 7.1 < V < 8.6 km s⁻¹. This subregion of the data cube contains most of the emission from the protostar and disk as well as selecting out the velocity range near the systemic velocity that is affected by opacity and spatial filtering. The noise can be described by a Gaussian, but it is correlated on the scale of 1''. Because the image is sampled with 0.2'' pixels, the degrees of freedom are reduced by a factor of 25, yielding 1056 degrees of freedom from the image region and velocity channels.

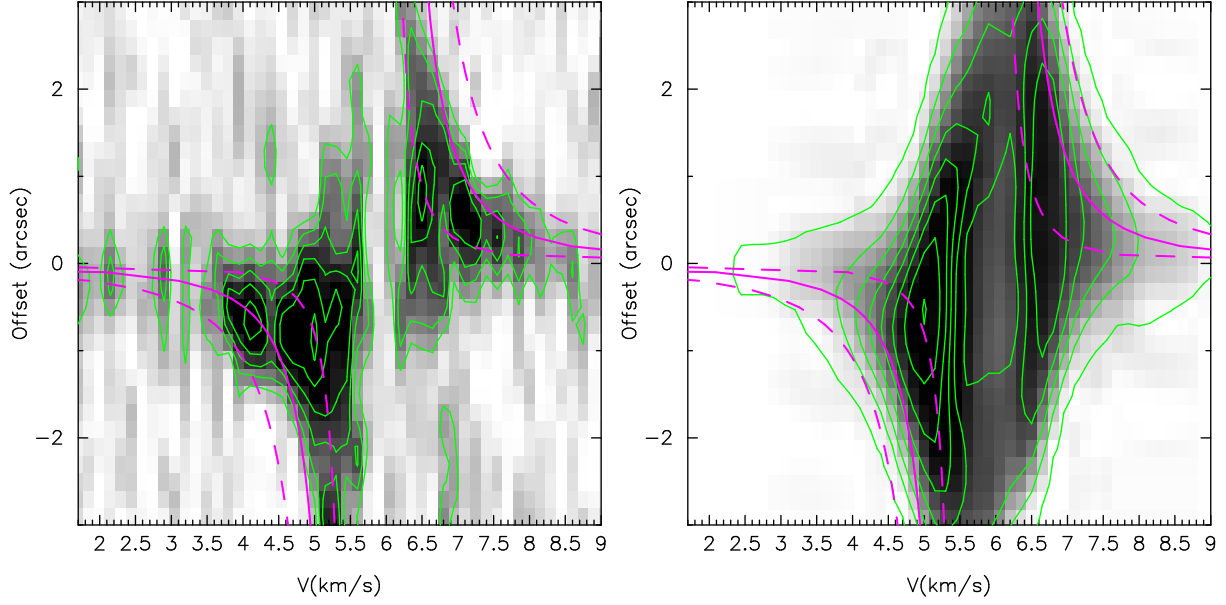
Unfortunately, the mass is not tightly constrained by the channel map analysis, likely due to abundance variations of ¹³CO and the low spatial resolution of the data compared to the size scale of emission. The reduced χ^2 values for each mass are given in Table S2, showing that masses between 0.075 and 0.175 M_{\odot} are equally probable (or improbable), with 0.125 M_{\odot} having the lowest reduced χ^2 . This comparison of the models to the data indicate a low mass, similar to the first method, giving further confidence that our first method using least-squares fitting is reliable.



SUPPLEMENTARY FIGURE 1. Channel maps of ^{13}CO emission in L1527. The velocity channels are 0.3 km s^{-1} wide and span the entire velocity range of emission detected in L1527. The line center velocity is 5.9 km s^{-1} where emission is absent due to spatial filtering and optical depth. At velocities within $\pm 1.3 \text{ km s}^{-1}$, the outflow is evident as the large “X” feature and the protostellar envelope is also visible in this velocity range. At higher velocities the emission is more compact and the red and blue-shifted emission appears on opposite sides, in the same direction as the disk and orthogonal to the outflow. This is strong evidence for the ^{13}CO to be tracing disk rotation. The contours start at 1.8 K (2σ) and increase in units of 2σ . The angular resolution of the channel maps has been tapered to $1.6'' \times 1.3''$ to better emphasize the large-scale outflow features.



SUPPLEMENTARY FIGURE 2. Radius versus Velocity plots of ^{13}CO emission for the L1527 observations (diamonds) the same measurements taken on the molecular line model (asterisks). Rotationally supported motion around a central point mass will have a velocity equal to $(GM/r)^{1/2}$. This function was fit to the observational and model data, finding a best fitting mass of $M_* = 0.19 \pm 0.04 M_\odot$. The velocity profile of the best fitting mass to the model and data is shown as the solid line. The actual mass of the model is $0.225 M_\odot$. The uncertainty in the observed data is derived from the channel width and the positional uncertainty of the Gaussian fit to the emission and the error in the position of the protostellar source. The data points of the model are entirely consistent with the observed data, including the flattening of radius at velocities less than 1.5 km s^{-1} . This flattening is due to the superposition of rotation velocities projected to our line of sight at large radii.



SUPPLEMENTARY FIGURE 3. Position-velocity diagrams of ^{13}CO in L1527 (left) and the model which agrees with our best-fitting mass ($M = 0.225 M_{\odot}$) (right) taken along the north-south axis of the disk/envelope. The PV structure of the observation closely resembles what is expected for rotating collapse, the deficit emission at 5.9 km s^{-1} is due to a combination of spatial filtering and self-absorption. The rotation of the disk is evident at the higher velocities within $\pm 1''$. The solid magenta lines are the Keplerian velocities for a $0.225 M_{\odot}$ object and the dashed magenta lines are Keplerian rotation curves for masses of 0.05 and $0.5 M_{\odot}$. The emission at radii greater than $1''$ is at a lower velocity than the best fitting mass because this is outside the likely disk radius and not rotationally supported; this emission dominated by infall velocities. The contours for the ^{13}CO data start at 2.5 K (5σ) and the contours on the left start at 0.5 K .

Supplementary Table 1. Least-Squares Mass Fits on the Models

Actual Model Mass (M_{\odot})	Fit Model Mass (M_{\odot})
0.025	0.06
0.05	0.04
0.075	0.11
0.1	0.11
0.125	0.13
0.15	0.14
0.175	0.15
0.2	0.17
0.225	0.19
0.25	0.21
0.275	0.22
0.3	0.24

The statistical uncertainties in the mass fit are typically $0.03 M_{\odot}$ and the data lack enough resolution to constrain masses less than $0.05 M_{\odot}$.

Supplementary Table 2. Results of Channel Map Fitting to the Data

Model Mass (M_{\odot})	Reduced χ^2
0.025	24.7
0.05	20.9
0.075	17.2
0.1	14.5
0.125	13.8
0.15	14.3
0.175	15.9
0.2	18.5
0.225	22.8
0.25	27.2
0.275	31.4
0.3	37.4

REFERENCES

- [1] Takakuwa, S. *et al.* A Keplerian Circumbinary Disk around the Protostellar System L1551 NE. *Astrophys. J.* **754**, 52 (2012).
- [2] Andre, P., Ward-Thompson, D. & Barsony, M. Submillimeter continuum observations of Rho Ophiuchi A - The candidate protostar VLA 1623 and prestellar clumps. *Astrophys. J.* **406**, 122–141 (1993).
- [3] Chandler, C. J. & Richer, J. S. The Structure of Protostellar Envelopes Derived from Submillimeter Continuum Images. *Astrophys. J.* **530**, 851–866 (2000).
- [4] Tobin, J. J. *et al.* Complex Structure in Class 0 Protostellar Envelopes. II. Kinematic Structure from Single-dish and Interferometric Molecular Line Mapping. *Astrophys. J.* **740**, 45 (2011).
- [5] Tobin, J. J., Hartmann, L. & Loinard, L. The Inner Envelope and Disk of L1527 Revealed: Gemini L'-band-scattered Light Imaging. *Astrophys. J. L.* **722**, L12–L17 (2010).

- [6] Foster, P. N. & Chevalier, R. A. Gravitational Collapse of an Isothermal Sphere. *Astrophys. J.* **416**, 303–+ (1993).
- [7] Jørgensen, J. K. *et al.* PROSAC: A Submillimeter Array Survey of Low-Mass Protostars. I. Overview of Program: Envelopes, Disks, Outflows, and Hot Cores. *Astrophys. J.* **659**, 479–498 (2007).
- [8] Maury, A. J. *et al.* Toward understanding the formation of multiple systems. A pilot IRAM-PdBI survey of Class 0 objects. *Astron. Astrophys.* **512**, A40+ (2010).
- [9] Andrews, S. M. & Williams, J. P. Circumstellar Dust Disks in Taurus-Auriga: The Submillimeter Perspective. *Astrophys. J.* **631**, 1134–1160 (2005).
- [10] Arce, H. G. & Sargent, A. I. The Evolution of Outflow-Envelope Interactions in Low-Mass Protostars. *Astrophys. J.* **646**, 1070–1085 (2006).
- [11] Ohashi, N., Hayashi, M., Ho, P. T. P. & Momose, M. Interferometric Imaging of IRAS 04368+2557 in the L1527 Molecular Cloud Core: A Dynamically Infalling Envelope with Rotation. *Astrophys. J.* **475**, 211–223 (1997).
- [12] Dapp, W. B. & Basu, S. Averting the magnetic braking catastrophe on small scales: disk formation due to Ohmic dissipation. *Astron. Astrophys.* **521**, L56 (2010).
- [13] Hennebelle, P. & Fromang, S. Magnetic processes in a collapsing dense core. I. Accretion and ejection. *Astron. Astrophys.* **477**, 9–24 (2008).
- [14] Yorke, H. W. & Bodenheimer, P. The Formation of Protostellar Disks. III. The Influence of Gravitationally Induced Angular Momentum Transport on Disk Structure and Appearance. *Astrophys. J.* **525**, 330–342 (1999).
- [15] Vorobyov, E. I. Embedded Protostellar Disks Around (Sub-)Solar Protostars. I. Disk Structure and Evolution. *Astrophys. J.* **723**, 1294–1307 (2010).
- [16] Joos, M., Hennebelle, P. & Ciardi, A. Protostellar disk formation and transport of angular momentum during magnetized core collapse. *Astron. Astrophys.* **543**, A128 (2012).
- [17] Simon, M., Dutrey, A. & Guilloteau, S. Dynamical Masses of T Tauri Stars and Calibration of Pre-Main-Sequence Evolution. *Astrophys. J.* **545**, 1034–1043 (2000).
- [18] Jørgensen, J. K. *et al.* PROSAC: a submillimeter array survey of low-mass protostars. II. The mass evolution of envelopes, disks, and stars from the Class 0 through I stages. *Astron. Astrophys.* **507**, 861–879 (2009).
- [19] Tobin, J. J., Hartmann, L., Calvet, N. & D’Alessio, P. Constraining the Envelope Structure of L1527 IRS: Infrared Scattered Light Modeling. *Astrophys. J.* **679**, 1364–1384 (2008).
- [20] Rodríguez, L. F. *et al.* Very Large Array Observations of Proper Motions in L1551 IRS 5. *Astrophys. J.* **583**, 330–333 (2003).
- [21] Hartmann, L., Cassen, P. & Kenyon, S. J. Disk Accretion and the Stellar Birthline. *Astrophys. J.* **475**, 770–785 (1997).
- [22] Evans, N. J. *et al.* The Spitzer c2d Legacy Results: Star-Formation Rates and Efficiencies; Evolution and Lifetimes. *Astrophys. J. Supp.* **181**, 321–350 (2009).
- [23] Dunham, M. M., Evans, N. J., Terebey, S., Dullemond, C. P. & Young, C. H. Evolutionary Signatures in the Formation of Low-Mass Protostars. II. Toward Reconciling Models and Observations. *Astrophys. J.* **710**, 470–502 (2010).
- [24] Narayanan, G., Snell, R. & Bemis, A. Molecular Outflows Identified in the FCRAO CO Survey of the Taurus Molecular Cloud. *ArXiv e-prints* (2012).
- [25] Bell, K. R., Cassen, P. M., Wasson, J. T. & Woolum, D. S. The FU Orionis Phenomenon and Solar Nebula Material. *Protostars and Planets IV* 897–926 (2000).
- [26] Andrews, S. M., Wilner, D. J., Hughes, A. M., Qi, C. & Dullemond, C. P. Protoplanetary Disk Structures in Ophiuchus. II. Extension to Fainter Sources. *Astrophys. J.* **723**, 1241–1254 (2010).
- [27] Tobin, J. J., Hartmann, L., Looney, L. W. & Chiang, H. Complex Structure in Class 0 Protostellar Envelopes. *Astrophys. J.* **712**, 1010–1028 (2010).

- [28] Woody, D. P. *et al.* CARMA: a new heterogeneous millimeter-wave interferometer. In Bradford, C. M. *et al.* (eds.) *Society of Photo-Optical Instrumentation Engineers (SPIE) Conference Series*, vol. 5498 of *Society of Photo-Optical Instrumentation Engineers (SPIE) Conference Series*, 30–41 (2004).
- [29] Ho, P. T. P., Moran, J. M. & Lo, K. Y. The Submillimeter Array. *Astrophys. J. L.* **616**, L1–L6 (2004).
- [30] Sault, R. J., Teuben, P. J. & Wright, M. C. H. A Retrospective View of MIRIAD. In R. A. Shaw, H. E. Payne, & J. J. E. Hayes (ed.) *Astronomical Data Analysis Software and Systems IV*, vol. 77 of *Astronomical Society of the Pacific Conference Series*, 433–+ (1995).
- [31] Pérez, L. M. *et al.* Atmospheric Phase Correction Using CARMA-PACS: High Angular Resolution Observations of the FU Orionis Star PP 13S*. *Astrophys. J.* **724**, 493–501 (2010).
- [32] Hogerheijde, M. R., van Dishoeck, E. F., Blake, G. A. & van Langevelde, H. J. Envelope Structure on 700 AU Scales and the Molecular Outflows of Low-Mass Young Stellar Objects. *Astrophys. J.* **502**, 315–+ (1998).
- [33] Kwon, W., Looney, L. W., Mundy, L. G., Chiang, H.-F. & Kemball, A. J. Grain Growth and Density Distribution of the Youngest Protostellar Systems. *Astrophys. J.* **696**, 841–852 (2009).
- [34] Ossenkopf, V. & Henning, T. Dust opacities for protostellar cores. *Astron. Astrophys.* **291**, 943–959 (1994).
- [35] Hartmann, L. Masses and mass distributions of protoplanetary disks. *Physica Scripta Volume T* **130**, 014012 (2008).
- [36] Melis, C. *et al.* Microwave Observations of Edge-on Protoplanetary Disks: Program Overview and First Results. *Astrophys. J. L.* **739**, L7+ (2011).
- [37] Brinch, C. & Hogerheijde, M. R. LIME - a flexible, non-LTE line excitation and radiation transfer method for millimeter and far-infrared wavelengths. *Astron. Astrophys.* **523**, A25 (2010).
- [38] Whitney, B. A., Wood, K., Bjorkman, J. E. & Wolff, M. J. Two-dimensional Radiative Transfer in Protostellar Envelopes. I. Effects of Geometry on Class I Sources. *Astrophys. J.* **591**, 1049–1063 (2003).
- [39] Ulrich, R. K. An infall model for the T Tauri phenomenon. *Astrophys. J.* **210**, 377–391 (1976).
- [40] Cassen, P. & Moosman, A. On the formation of protostellar disks. *Icarus* **48**, 353–376 (1981).
- [41] Terebey, S., Shu, F. H. & Cassen, P. The collapse of the cores of slowly rotating isothermal clouds. *Astrophys. J.* **286**, 529–551 (1984).
- [42] Tobin, J. J. (2012). In preparation.
- [43] Lee, J., Bergin, E. A. & Evans, N. J., II. Evolution of Chemistry and Molecular Line Profiles during Protostellar Collapse. *Astrophys. J.* **617**, 360–383 (2004).